



Cite this: *Nanoscale*, 2019, **11**, 11099

Received 28th March 2019,
 Accepted 21st May 2019

DOI: 10.1039/c9nr02681a

rsc.li/nanoscale

Predicting two-dimensional semiconducting boron carbides†

Xinxin Tian,^a Xiaoyu Xuan,^b Meng Yu,^c Yuewen Mu,^a Hai-Gang Lu,^a Zhuhua Zhang^{*b} and Si-Dian Li^{*a}

Carbon and boron can mix to form numerous two-dimensional (2D) compounds with strong covalent bonds, yet very few possess a bandgap for functional applications. Motivated by the structural similarity between graphene and recently synthesized borophene, we propose a new family of semiconducting boron carbide monolayers composed of B_4C_3 pyramids and carbon hexagons, denoted as $(B_4C_3)_m(C_6)_n$ (m, n are integers) by means of the global minimum search method augmented with first-principles calculations. These monolayers are isoelectronic to graphene yet exhibit increased bandgaps with decreasing n/m , due to the enhanced localization of boron multicenter bonding states as a consequence of the electronic transfer from boron to carbon. In particular, the B_4C_3 monolayer is even more stable than the previously synthesized BC_3 monolayer and has a direct bandgap of 2.73 eV, with the promise for applications in optical catalysis and optoelectronics. These results are likely to inform the on-going effort on the design of semiconducting 2D materials based on other light elements.

Introduction

Light elements, such as boron, carbon, and nitrogen, are known for their ability to form a wide variety of elemental crystals and compounds with strong covalent bonds. When confined to two-dimensional (2D) spaces, these elements give birth to atomically thin materials that stand out in terms of superlative mechanical properties and fantastic electronic properties. 2D carbon, *i.e.* graphene, adopts a honeycomb lattice with novel Dirac fermions for potential application in a number of technical fields.^{1–7} As a boron analogue of graphene, 2D boron, called borophene,^{8,9} was proposed as a network of B-filled hexagons in the otherwise honeycomb lattice.¹⁰ Following theoretical predictions, borophene has been synthesized on Ag(111) substrates by two recent independent experiments and is known to be the thinnest metallic material.^{11,12} Aside from these elemental 2D materials, many blends of light elements exhibit their 2D suits, such as 2D nitrides and oxides. However, most reported 2D materials fully composed of light elements either lack a bandgap or are electrically insulating, severely limiting their potential applications in functional devices that require semiconducting properties.

Among the diverse blends of light elements, 2D boron carbides have attracted special interest not only because bulk boron carbides are important superhard materials but also because marked similarity exists between carbon and boron chemistry. A notable example is the BC_3 monolayer, in which each carbon hexagon is surrounded by six boron atoms. Experimentally, the graphene-like BC_3 monolayer was confirmed by electron diffraction data¹³ and has been synthesized by hot filament chemical vapor deposition methods.^{14,15} While the BC_3 monolayer is semiconducting, it has an indirect bandgap¹⁶ that limits the performance of, for example, photoelectronic devices. Later on, Luo *et al.*¹⁷ have proposed a series of boron carbide monolayers based on a structural search by the particle swarm optimization (PSO) algorithm. With

^aInstitute of Molecular Science, Key Laboratory of Materials for Energy Conversion and Storage of Shanxi Province, Shanxi University, Taiyuan 030006, P. R. China. E-mail: ywmu@sxu.edu.cn, lisdian@sxu.edu.cn

^bState Key Laboratory of Mechanics and Control of Mechanical Structures, Key Laboratory for Intelligent Nano Materials and Devices of Ministry of Education and Institute of Nano Science, Nanjing University of Aeronautics and Astronautics, Nanjing 210016, China. E-mail: chuwarzhang@nuaa.edu.cn

^cSchool of chemistry and chemical engineering, Yulin University, Yulin, 719000, P. R. China

† Electronic supplementary information (ESI) available: Other structural details of the B_4C_3 monolayer; optimized low-lying isomers of B_4C_3 monolayers; optimized geometries and band structures of the $(B_4C_3)_m(C_6)_n$ ($n/m = 1–7$) family; phonon dispersion frequencies of the $(B_4C_3)_3(C_6)_6$ monolayer; π bonding patterns of α -sheet and BC_3 monolayers; typical nanotubes rolled from the B_4C_3 sheet; formation energies of B_mC_n monolayers and the $(B_4C_3)_m(C_6)_n$ ($n/m = 1–7$) family; the diameters, average formation energies and bandgaps of B_4C_3 nanotubes are collected. The animations of the MD simulations of the B_4C_3 monolayer at 1000 K. (AVI). The .cif files of low-lying 2D B_4C_3 sheets and 1D nanotubes (.zip). See DOI: 10.1039/c9nr02681a

increasing boron concentration, the energetically preferred B–C monolayer structure evolves from a homogenous honeycomb structure to a heterostructure composed of carbon and boron domains. However, all the newly proposed 2D B–C compounds turn out to be metallic.^{18,19} A recent theory suggested that the thermal stability of graphene cannot be substantially undermined by boron doping up to a concentration of 33% (or with a formula of BC₂), but a 2D B–C semiconductor with a direct bandgap is yet to be explored.

In this Communication, we found a new family of 2D B–C monolayers that not only exhibit high stability but also uniformly offer direct bandgaps, as shown by first-principles calculations combined with the global minimum search. The idea was provoked by a designed B₄C₃H₆ molecule with a three-fold symmetry which possesses similar aromaticity to benzene (C₆H₆). The B₄C₃H₆ molecule then serves as a precursor to form a 2D B₄C₃ monolayer with a direct bandgap of 2.73 eV due to the broken symmetry between B and C sublattices. Furthermore, the B₄C₃ units can alloy with C₆ rings to form a large family of 2D B–C monolayers, formulated as (B₄C₃)_m(C₆)_n (*m*, *n* are integers), which exhibit a decreased band gap with increasing *n/m*, down to the case of graphene (*n/m* = ∞) with zero bandgap. Calculated optical and electronic properties, along with the variable bandgap by changing compositions, suggest these B–C monolayers to be compelling contenders for next-generation electronic and optoelectronic devices.

Methods

The calculations were performed within the framework of density functional theory, as implemented in the Vienna *ab initio* simulation package (VASP) code.^{20,21} The electron-ion interaction was described by the projector augmented wave (PAW) method,^{22,23} and the exchange correlation energy was treated within the generalized gradient approximation of the Perdew–Burke–Ernzerhof functional (GGA-PBE).^{24,25} The cutoff energy of the plane wave basis is set to 400 eV. Atomic structures are fully relaxed using the conjugate gradient method until the force on each atom was less than 0.01 eV Å⁻¹ and the energy difference less than 10⁻⁴ eV. For the global structural search, the Brillouin zones were sampled with 0.5 Å⁻¹ spacing by the Monkhorst–Pack scheme, and the vacuum thickness between two monolayers in periodic images was set to 10 Å; we adopted 0.1 Å⁻¹ spacing and a vacuum thickness of 15 Å for further structural optimization to establish the reliable global minima. The corresponding grids of *k*-point sampling are 8 × 13 × 1 for geometry optimization and 9 × 15 × 1 for electronic structure calculations. The global minimum search based on the PSO algorithm was implemented with the Crystal Structure Analysis by Particle Swarm Optimization (CALYPSO) package.²⁶ The hybrid Heyd–Scuseria–Ernzerhof (HSE06) functional²⁷ was employed to calculate the electronic structures of B–C monolayers. The phonon spectra are calculated using the finite displacement method with the Phonopy code at the PBE level.²⁸

For calculating optical properties, we use an energy cutoff of 500 eV and set *k*-point sampling to be 12 × 20 × 1. The number of empty conduction bands was set to be triple that of occupied valence bands. The optical absorption coefficient $\alpha(E)$ is calculated through the following formula:

$$\alpha(E) = \frac{\sqrt{2}E \left[\sqrt{\text{real}(\epsilon)^2 + \text{imag}(\epsilon)^2} - \text{real}(\epsilon) \right]^{1/2}}{hc}$$

where *E* is the energy, $\text{real}(\epsilon)$ and $\text{imag}(\epsilon)$ are the real and imaginary parts of the dielectric function, respectively. The molecular dynamics simulations were performed for 10 ps with the CP2K software suite.²⁹ We used a 2 × 3 × 1 supercell and the NVT ensemble with a time step of 1 fs.

Results and discussion

Fig. 1a presents the atomic structure of the proposed C_{3v} B₄C₃H₆ molecule which is isoelectronic to a benzene molecule C₆H₆. B₄C₃H₆ contains a hexa-coordinate B center, denoted as η⁶-B. Most notably, the electronic structure of B₄C₃H₆ is markedly similar to benzene (C₆H₆), especially by three completely delocalized π orbitals shown in Fig. 1a. It is known that graphene is made of interconnected C₆ building blocks, we conceive that a new 2D material can be formed from the B₄C₃ precursor. This is further supported by the fact that the B₄C₃

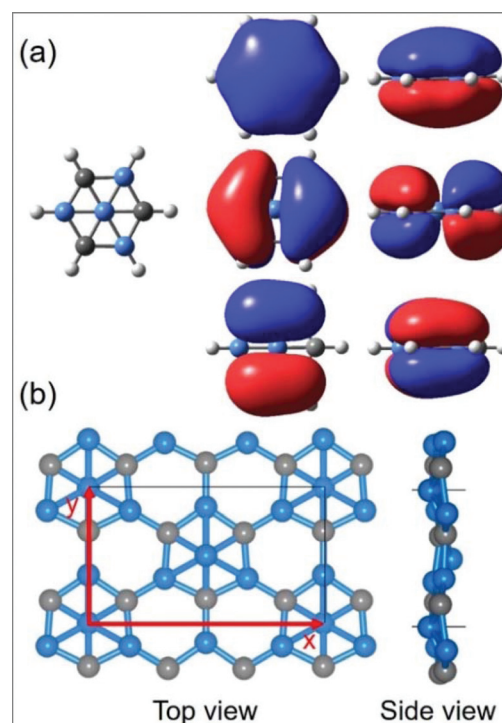


Fig. 1 Top and side views of (a) the optimized structure and canonical molecular orbitals of the three 7c–2e π bonds of B₄C₃H₆; (b) the most stable structure of the 2D B₈C₆ unit cell (blue ball for B, grey ball for C, and white ball for H).

motif is also a minimum without imaginary frequency and was predicted to be the lowest energy state among the B_4C_3 isomers.³⁰ Note that the B_4C_3 precursor completely differs from a previously proposed planar B_4C_3 species,³¹ which has a carbon atom centred at the hexagon and is thus unstable.

Fig. 1b shows the atomic structure of a graphene-like B_4C_3 monolayer, which exhibits a $Pmn2_1$ symmetry (No. 31) with a rectangular primitive cell. The primitive cell contains two B-filled B_3C_3 rings, forming a B_8C_6 . The lattice parameters are $a = 8.10$, $b = 4.67$ Å. Furthermore, boron and carbon atoms arrange alternately along the periphery of each hexagon, with two η^6 -B atoms protruding upward and downward, respectively, from the plane, resulting in an off-plane buckling of 0.75 Å. Interestingly, each C atom is tetra-coordinated, forming a planar tetracoordinate carbon (ptC) akin to the ptC motif in earlier predicted B_2C ,¹⁷ TiC ,³² and BeC ³³ monolayers as well as Cu-decorated graphene edges.³⁴ The chemistry on the ptC has been thoroughly discussed in a previous review.³⁵ The center B atom is hexa-coordinated while the periphery B atom is tetra-coordinated. These coordinations are somewhat similar to those in 2D FeB_6 ³⁶ and 2D AlB_6 .³⁷ The latter contains quasiplanar tetra-coordinated and buckled hexa-coordinated B atoms in B_6 -ptAl- B_6 arrays. The structure of the B_4C_3 monolayer also resembles the 2D X_2Y ($X = Cu/Ni$, $Y = Si/Ge/P/As$) materials with a hole density of $2/3$.^{38–41}

The B_4C_3 monolayer is further confirmed to be the global minimum by an extensive PSO search. The obtained 10 low-lying structures of B_4C_3 isomers in the energy-configuration spectrum are provided in Fig. S1.† It is found that the B_4C_3 monolayer is more stable than the second-stable structure by 200 meV per B_4C_3 unit, rendering a deep global minimum for the monolayer. We also calculate the average cohesive energy per atom as $E_{coh} = (n_C E_C + m_B E_B - E_{monolayer}) / (n_C + m_B)$, where $E_{monolayer}$, E_C and E_B are the total energy of the B_4C_3 isomers and individual C and B atoms, respectively, and n_C and m_B are the numbers of C and B atoms in the unit cell, respectively. For the 10 structures, E_{coh} ranges from 6.52 to 6.63 eV per atom, close to 7.20 eV per atom for the h-BN⁴² and 6.10 eV per atom for the 2D AlB_6 ³⁷ yet distinctly higher than 2.98–4.80 eV

per atom for a series of 2D X_2Y ($X = Cu/Ni$, $Y = Si/Ge/P/As$).^{38–41} The B_4C_3 monolayer shows the highest E_{coh} of 6.63 eV per atom with the strongest B–C bonds among these structures.

The calculated phonon spectrum (Fig. 2a) of the B_4C_3 monolayer does not show any imaginary frequency, confirming its dynamical stability. The highest frequency reaches up to 1400 cm^{-1} which is attributed to the in-plane oscillation modes of B–C bonds. This frequency is only slightly lower than that of the h-BN⁴³ yet significantly higher than those in 2D AlB_6 and 2D X_2Y ($X = Cu/Ni$, $Y = Si/Ge/P/As$),^{37–41} again reflecting a strong bonding network of the B_4C_3 monolayer. We also performed *ab initio* molecular dynamics simulations with a 2×3 supercell. No significant structural distortion and bond breakage appears in the structure of the B_4C_3 monolayer throughout 10 ps simulations at a temperature up to 1000 K, confirming that the monolayer is thermally stable as well. The animations of the dynamic simulations are provided as an appendix.

The relative stability of the B_4C_3 monolayer to 7 other B–C monolayers is further evaluated by comparing their formation energies (Fig. 2b). We refer the structures with 7 other compositions to ref. 17. The formation energy is calculated as $E_f = (E_t - n_C \mu_C - m_B \mu_B) / (n_C + m_B)$, where E_t , μ_B , and μ_C are the total energies of $B_m C_n$ monolayers, chemical potential of boron α -sheet and graphene, respectively. In the binary phase diagram, the formation energy of different composition compounds is negative when the reaction of forming such compounds is exothermic. In contrast, the formation energy of all 2D boron carbides is positive, since C and B intrinsically tend to undergo phase separation. However, the positive formation energy does not mean it is unstable but indicates its metastable nature. Once these 2D compounds are formed under certain conditions (*e.g.* high temperatures), the strong covalent B–C bonds should prevent them from destabilization. Among the B–C monolayers, the B_4C_3 monolayer has the smallest E_f (0.06 eV per atom), significantly lower than those of the BC_5 (0.09 eV per atom) and BC_3 (0.10 eV per atom) monolayers. These results suggest that the B_4C_3 monolayer is probably the most stable 2D B–C compound. When using the experimentally realized β_{12} and χ_3 borophene as references, E_f of the

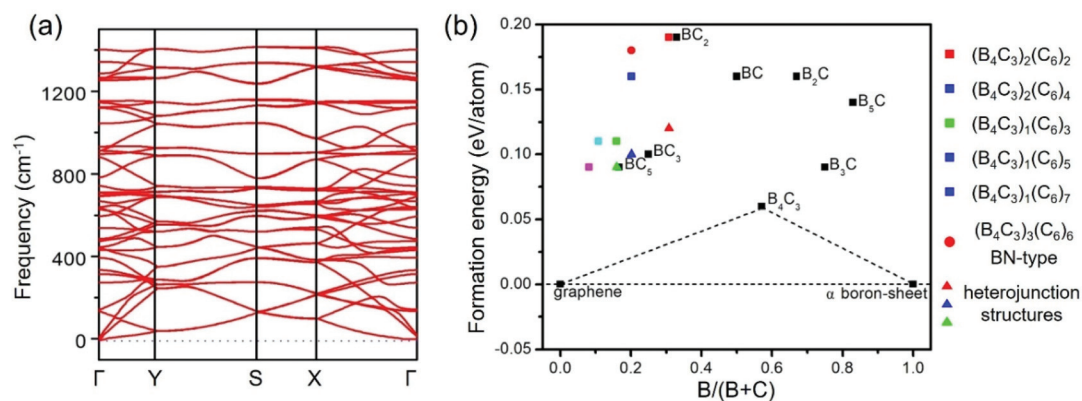


Fig. 2 (a) The phonon dispersion frequencies of the B_8C_6 unit cell. (b) Formation energies per atom for 2D $B_m C_n$ monolayers with respect to graphene and boron α -sheet. Heterojunction structures represent the monolayers with separated carbon and boron domains.

B_4C_3 monolayer becomes even lower, 0.03 and 0.04 eV per atom, respectively. Since the BC_3 monolayer has been synthesized by doping boron into graphene on Cu foil,¹⁴ the B_4C_3 monolayer holds a great possibility of being synthesized on properly selected substrates in the near future.

Given the high stability of the B_4C_3 monolayer, the B_4C_3 unit can be further alloyed with the C_6 unit (*i.e.* benzene ring) to form a rich variety of B–C monolayers. Acting along this way, we design a family of $(B_4C_3)_m(C_6)_n$ monolayers composed of B_4C_3 and C_6 units. Their structures and formation energies are shown in Fig. S2† and Fig. 2b, respectively. While these monolayers are less stable than their corresponding in-plane heterostructures composed of graphene and B_4C_3 domains, they prove to be structurally and dynamically stable by their low formation energies and all-positive phonon frequencies (Table S1 and Fig. S3†). For the ease of discussion, we focus on the B_4C_3 monolayer first and discuss the $(B_4C_3)_m(C_6)_n$ monolayers later.

Next, we examine the electronic properties of the B_4C_3 monolayer by showing its band structure and density of states (DOS) in Fig. 3a. The B_4C_3 monolayer is semiconducting with a direct bandgap of 2.73 eV. The near-gap states are primarily derived from C and B 2p states. B atoms contribute more above the Fermi level while C atoms contribute more below

the Fermi level. To our knowledge, this is the first report of a 2D B–C semiconductor with a direct bandgap, distinguished from the semi-metallic graphene,¹ metallic borophene,¹⁰ and other B–C monolayers.^{16,17} The valence band maximum (VBM) and conduction band minimum (CBM) are both located at the Γ point.

There are double degenerate states at the valence band maximum, denoted as VBM(I) and VBM(II), respectively. The spatial distribution of partial charge density for these VBM is predominantly from π orbitals on carbon atoms while that for the CBM is from the π^* orbitals on boron atoms, as illustrated in Fig. 4. The bandgap can thus be interpreted as a consequence of electronic transfer from B atoms to C atoms, which results in asymmetry of the on-site potential between B and C sublattices. As a result, the π and π^* states are localized spatially in separate regions, similar to the case in h-BN. This mechanism for bandgap opening differs from that in the BC_3 monolayer, in which the indirect bandgap is attributed to the localization of six-center two-electron π -bonds.⁴⁴

It is worth mentioning that the CBM shows substantial overlap with the VBM *via* one C atom along the x direction and one C atom along the y direction. The overlap between the CBM and VBM alleviates the electronic localization and facilitates electron transport. The calculated values of effective mass m^*

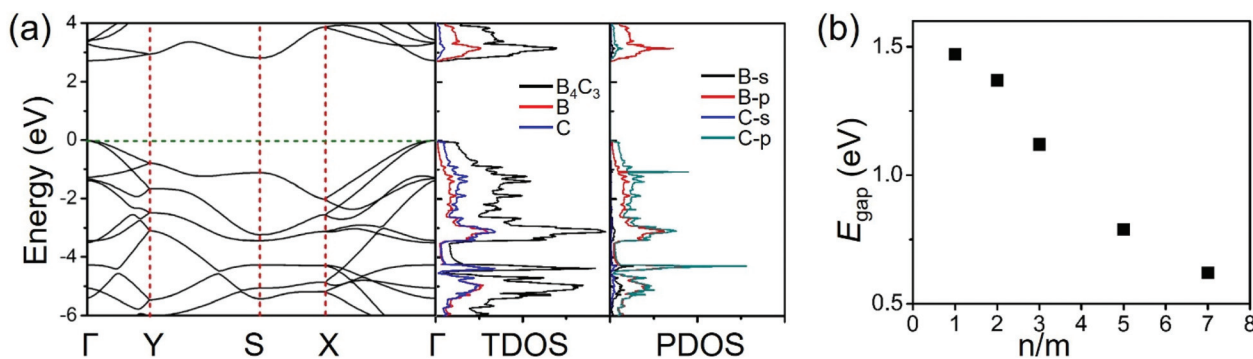


Fig. 3 (a) Band structure, total density of state (TDOS) and partial density of state (PDOS) of the B_4C_3 monolayer calculated using the HSE06 functional. (b) Band gap of the $(B_4C_3)_m(C_6)_n$ monolayer versus n/m .

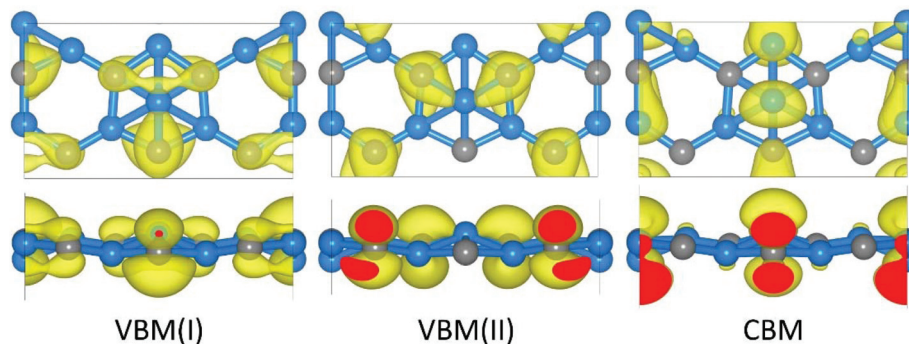


Fig. 4 Top and side views of isosurface plots ($0.005 \text{ e}\text{\AA}^{-3}$) of the partial charge densities corresponding to the VBM and CBM for the B_4C_3 monolayer. Carbon and boron atoms are colored grey and blue, respectively.

Table 1 Calculated effective mass m^* in units of free electron mass m_0 , and mobility μ for the B_4C_3 monolayer along x and y directions. The subscripts follow e (electron) and h (hole)

Direction	m_e^*	m_h^*	μ_e ($10^3 \text{ cm}^2 \text{ V}^{-1} \text{ s}^{-1}$)	μ_h ($10^3 \text{ cm}^2 \text{ V}^{-1} \text{ s}^{-1}$)
x	2.30	0.58	0.52	16.85
y	0.29	0.43	3.66	20.81

and mobility μ for the B_4C_3 monolayer are summarized in Table 1. Notably, the B_4C_3 monolayer offers rather high mobility of charge carriers, reaching up to $2.1 \times 10^4 \text{ cm}^2 \text{ V}^{-1} \text{ s}^{-1}$ for hole carriers along the y direction. This value exceeds that of silicon⁴⁵ and approaches that of 2D black phosphorus.^{46,47} Interestingly, the monolayer exhibits strong electronic anisotropy and asymmetry between electron and hole carriers. The hole mobility is much higher than the electron mobility, while the mobility in the y direction is apparently higher than those in the x direction. These results suggest that the B_4C_3 monolayer is likely to be a p-type semiconductor and that the carriers will tend to transport along the y direction.

To gain a deeper insight into an electronic configuration in the B_4C_3 monolayer, we performed an adaptive natural density partitioning (AdNDP)⁴⁸ bonding analysis using the fragmentation approach. To capture all structural characteristics in the B_4C_3 monolayer, a large $B_{28}C_{21}$ fragment terminated with hydrogen was employed. As shown in Fig. 5, we identify in this fragment 18 $2c-2e$ B-H or C-H σ -bonds, 12 $2c-2e$ B-C σ -bonds, 42 $3c-2e$ σ bonds, and 21 $7c-2e$ π bonds. All the occupation numbers (ONs) of $2c-2e$ and $3c-2e$ σ bonds are greater

than 1.90 $|e|$. Specifically, the seven B-filled B_4C_3 hexagons are interconnected by $2c-2e$ B-C σ -bonds, while each B_4C_3 unit possesses 6 $3c-2e$ σ bonds involving two periphery atoms and one center atom. The remaining six electrons are distributed in three $7c-2e$ π bonds with ON $> 1.80 |e|$, similar to that in a C_6H_6 molecule. The ON values of the $7c-2e$ π bonds (1.84–2.00 $|e|$) exceed the corresponding values in graphene (1.83–1.88 $|e|$)⁴⁹ and the boron α -sheet (1.72 $|e|$).⁵⁰ Therefore, in the B_4C_3 monolayer, the filled B_4C_3 hexagon atoms are braided by 3 delocalized $7c-2e$ π -bonds, 6 $3c-2e$ σ bonds, and 6 $2c-2e$ B-C σ -bonds, while the empty hexagons have no π -occupation (Fig. 6a). Such a bonding pattern is similar to that of the BC_3 monolayer, where 3 $6c-2e$ π bonds are found on each C_6 hexagon and the π -bond on each C_4B_2 hexagon is broken by boron atoms (Fig. S4†).⁴⁴ In contrast, for graphene⁴⁹ (Fig. 6b) and boron α -sheets⁵⁰ (Fig. S4†), the π bonds are uniformly distributed throughout the whole materials.

The direct bandgap makes the B_4C_3 monolayer a promising candidate for applications in photocatalysis. We first calculated the dielectric function (in-plane polarization) of the monolayer. As shown in Fig. 7a, the optical adsorption is found to arise at ~ 1.4 eV (almost identical to the PBE bandgap of 1.34 eV) and quickly reach a peak at 3.1 eV, indicating that the B_4C_3 monolayer exhibits large absorption in the region from blue to ultraviolet. The coefficient α at 3.1 eV is comparable to those of 2D black phosphorus⁵¹ and exhibits slight anisotropy between the x and y directions. The results obtained using the HSE06 functional yet with sparser k -point sampling (due to large computational cost) are qualitatively the same (except that the peak undergoes a blue-shift).

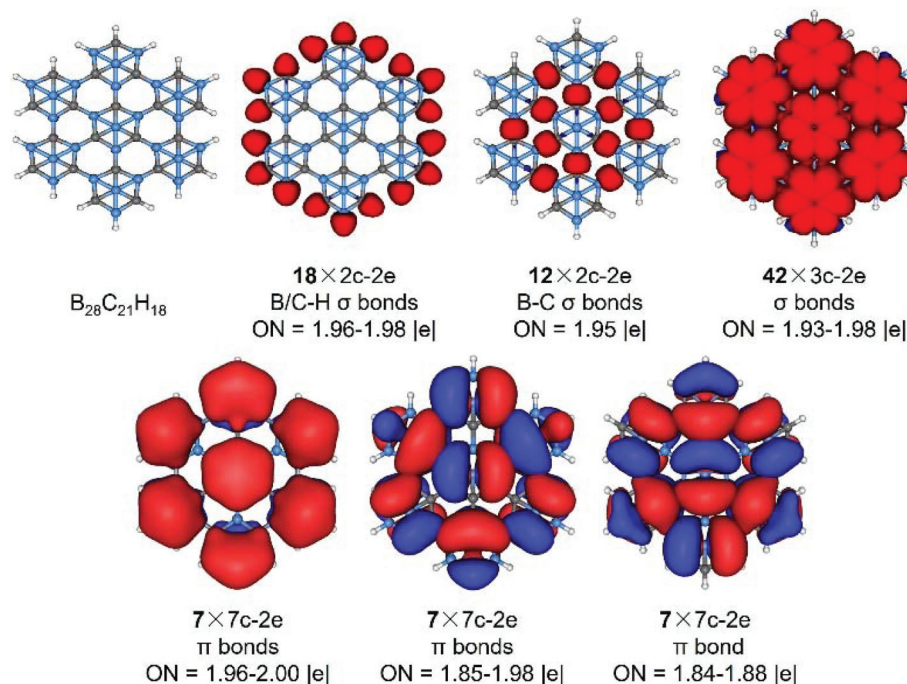


Fig. 5 AdNDP chemical bonding analysis of a $B_{28}C_{21}H_{18}$ molecule, which represents a segment of the B_4C_3 monolayer.

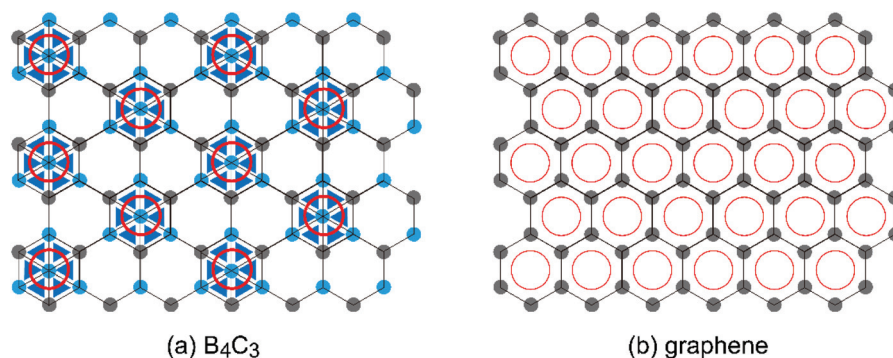


Fig. 6 The π bonding patterns of the (a) B_4C_3 and (b) graphene monolayers. The triangle represents a $3c-2e$ σ bond. The thin and thick red circles represent one and three delocalized π bonds, respectively. Carbon and boron atoms are colored grey and blue, respectively.

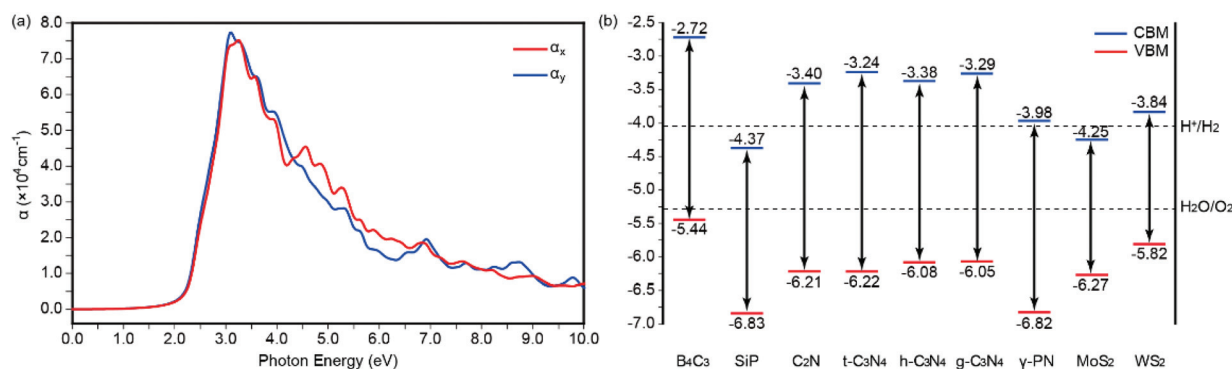


Fig. 7 (a) Optical absorption coefficients of the B_4C_3 monolayer along the x and y directions. (b) Diagram of the band edge levels of various 2D semiconducting materials, along with redox potentials of H_2O splitting at pH = 7.

We next examine the levels of the VBM and CBM for the B_4C_3 monolayer, based on HSE06 calculations (Fig. 7b). The reduction potentials of H^+/H_2 and oxidation potential of O_2/H_2O at pH = 7 are -4.03 eV and -5.26 eV respectively, which are key to water-splitting materials driven by visible light.⁵² The bandgap of the B_4C_3 monolayer is comparable to those of SiP, C_2N , C_3N_4 , and PN light element materials^{53–57} and higher than those of MoS₂ and WS₂,⁵⁸ but their bandalignments relative to the vacuum level varies in a wide range. For the B_4C_3 monolayer, the levels of CBM and VBM are -2.72 and -5.44 V, respectively (Fig. 7b). Its bandgap straddles the redox potential of H_2O splitting, indicating the photocatalytic activity.

Under optical excitation, a heterostructure made of 2D materials with a suitable match of bandgaps allows for an efficient separation of hole and electron carriers, which then can catalyze related reactions in a manner similar to electrocatalysis. In this regard, the B_4C_3 monolayer can be assembled with other 2D semiconductors to form vertical heterostructures, towards achieving improved photocatalytic performance. The type II hetero-structures with staggered band alignment at the interface are required for charge carrier separation to enable the photocatalytic activity.⁵⁹ The oxidation and reduction reactions take place separately in two components of heterostructures. Fig. 7b shows that a couple of 2D

semiconductors can form type II heterostructures with the B_4C_3 monolayer. Among them, the B_4C_3/C_2N and B_4C_3/C_3N_4 structures should have less minimization on the oxidation and reduction powers of charge transfer than B_4C_3/SiP , B_4C_3/γ -PN, B_4C_3/MoS_2 , and B_4C_3/WS_2 ones do. Thus, the B_4C_3/C_2N and B_4C_3/C_3N_4 heterostructures potentially have a photocatalytic activity to serve as metal-free photocatalysts, but the practical performance needs to be verified by future experiments.

Beyond the monolayer structures, one-dimensional nanotubes can be rolled up from the B_4C_3 monolayer. As shown in Fig. 1b, the lattice vectors for rolling the monolayer into a nanotube are x and y , with an angle of $\gamma = 90^\circ$. When rolling along the x direction, a zigzag nanotube can be obtained and indexed as $(n, 0)$, while a $(0, m)$ armchair nanotube can be obtained when rolling along the y direction. The armchair nanotube can also be obtained by rolling along a diagonal direction, notated as (n, n) . We studied the two families of B_4C_3 nanotubes with diameters of 5–18 Å. The structures of the armchair $(0, 6)$ and zigzag $(5, 0)$ are shown in Fig. S5† as examples.

Apparently, E_f of nanotubes is higher than the B_4C_3 monolayer due to the curvature effect. The band structures of nanotubes were calculated at the HSE06 level and are shown in Fig. S6 and Table S2.† All studied nanotubes remain semicon-

ducting. For the zigzag ($n, 0$) tubes, the bandgap increases from 0.61 eV to 1.82 eV as the diameter increases from 5.39 Å to 13.03 Å. The bandgap of armchair ($0, n$) tubes shows no clear monotonic dependence on the tube size, but is generally larger than those of zigzag ($n, 0$) tubes. The bandgap of the ($0, 5$) tube is close to that of the B_4C_3 monolayer (2.65 vs. 2.73 eV). This behavior differs from that of boron nanotubes, whose bandgap decreases with increasing tube diameter and which change from semiconducting to metallic when the diameter is thicker than 17 Å.⁶⁰

In addition to the B_4C_3 monolayer, we have also studied the electronic properties of other $(B_4C_3)_m(C_6)_n$ monolayers. Our extensive calculations at the HSE06 level show that the monolayer has an increased bandgap with decreasing n/m (Fig. 3b and Fig. S7†), due to enhanced localization of delocalized π bonds as a consequence of electronic transfer from boron to carbon. For example, the $(B_4C_3)_1(C_6)_3$ and $(B_4C_3)_3(C_6)_6$ monolayers (see structure in Fig. S2†) have direct bandgaps of 1.12 and 1.17 eV, respectively, both close to that of silicon. If these monolayers were synthesized, their bandgap sizes, combined with the nature of the direct bandgap, would open a wealth of opportunity for applications in nanoelectronics and photoelectronics.

Conclusions

In summary, we have found a highly stable 2D B_4C_3 monolayer that is a semiconductor with a direct bandgap of 2.73 eV, using first-principles calculations combined with the global minimum search method. It has a well-mixed distribution of hollow and B-filled B_3C_3 hexagons. The B_4C_3 monolayer is expected to have higher stability than the BC_3 monolayer that has been experimentally synthesized. Chemical bonding analyses disclose that boron still preserves the property of forming multicenter σ -bonds, and π -bonds are identified for every B-filled hexagon, resembling that in the BC_3 monolayer but unlike that in graphene. Nanotubes derived from the B_4C_3 monolayer remain semiconducting, but the dependence of the band gap versus tube diameter differs from that of pure boron nanotubes. The B_4C_3 units can be further mixed with C_6 rings to form a family of $(B_4C_3)_m(C_6)_n$ monolayers with excellent electronic properties. The new design strategy demonstrated here will be applicable to other elements to yield more 2D materials with outstanding electronic properties and functionalities.

Conflicts of interest

There are no conflicts to declare.

Acknowledgements

This work was supported by the National Natural Science Foundation of China (21720102006, U1510103, 11504213 and 21603129), the Shanghai Supercomputing Center and the

Supercomputing Center of Shanxi University. Z. Z. acknowledged the support of NSFC (11772153), the Research Fund of State Key Laboratory of MCMS (MCMS-0417G01) and the Fundamental Research Funds for the Central Universities (NE2018002). We thank Prof. Huajin Zhai, Prof. Haijun Jiao and Prof. Xiaodong Wen for valuable discussions.

References

- 1 K. S. Novoselov, A. K. Geim, S. V. Morozov, D. Jiang, M. I. Katsnelson, I. V. Grigorieva, S. V. Dubonos and A. A. Firsov, *Nature*, 2005, **438**, 197.
- 2 A. K. Geim and K. S. Novoselov, *Nat. Mater.*, 2007, **6**, 183.
- 3 M. D. Stoller, S. Park, Y. Zhu, J. An and R. S. Ruoff, *Nano Lett.*, 2008, **8**, 3498.
- 4 K. Mullen and J. P. Rabe, *Acc. Chem. Res.*, 2008, **41**, 511.
- 5 Q. Bao and K. P. Loh, *ACS Nano*, 2012, **6**, 3677.
- 6 F. Bonaccorso, Z. Sun, T. Hasan and A. C. Ferrari, *Nat. Photonics*, 2010, **4**, 611.
- 7 C. N. Rao, A. K. Sood, K. S. Subrahmanyam and A. Govindaraj, *Angew. Chem., Int. Ed.*, 2009, **48**, 7752.
- 8 I. Boustani, *Surf. Sci.*, 1997, **370**, 355.
- 9 Z. A. Piazza, H. S. Hu, W. L. Li, Y. F. Zhao, J. Li and L. S. Wang, *Nat. Commun.*, 2014, **5**, 3113.
- 10 H. Tang and S. Ismail-Beigi, *Phys. Rev. Lett.*, 2007, **99**, 115501.
- 11 A. J. Mannix, X. F. Zhou, B. Kiraly, J. D. Wood, D. Alducin, B. D. Myers, X. Liu, B. L. Fisher, U. Santiago, J. R. Guest, M. J. Yacaman, A. Ponce, A. R. Oganov, M. C. Hersam and N. P. Guisinger, *Science*, 2015, **350**, 1513.
- 12 B. Feng, J. Zhang, Q. Zhong, W. Li, S. Li, H. Li, P. Cheng, S. Meng, L. Chen and K. Wu, *Nat. Chem.*, 2016, **8**, 563.
- 13 J. Kouvetakis, R. B. Kaner, M. L. Sattler and N. Bartlett, *J. Chem. Soc., Chem. Commun.*, 1986, **24**, 1758.
- 14 A. Jafari, M. Ghoranneviss and A. S. Elahi, *J. Cryst. Growth*, 2016, **438**, 70.
- 15 H. Yanagisawa, T. Tanaka, Y. Ishida, M. Matsue, E. Rokuta, S. Otani and C. Oshima, *Phys. Rev. Lett.*, 2004, **93**, 177003.
- 16 D. Tománek, R. M. Wentzcovitch, S. G. Louie and M. L. Cohen, *Phys. Rev. B: Condens. Matter Mater. Phys.*, 1988, **37**, 3134.
- 17 X. Luo, J. Yang, H. Liu, X. Wu, Y. Wang, Y. Ma, S.-H. Wei, X. Gong and H. Xiang, *J. Am. Chem. Soc.*, 2011, **133**, 16285.
- 18 Q. Hu, Q. Wu, Y. Ma, L. Zhang, Z. Liu, J. He, H. Sun, H. T. Wang and Y. Tian, *Phys. Rev. B: Condens. Matter Mater. Phys.*, 2006, **73**, 214116.
- 19 X. Wu, Y. Pei and X. C. Zeng, *Nano Lett.*, 2009, **9**, 1577.
- 20 G. Kresse and J. Furthmüller, *Comput. Mater. Sci.*, 1996, **6**, 15.
- 21 G. Kresse and J. Furthmüller, *Phys. Rev. B: Condens. Matter Mater. Phys.*, 1996, **54**, 11169.
- 22 P. E. Blöchl, *Phys. Rev. B: Condens. Matter Mater. Phys.*, 1994, **50**, 17953.
- 23 G. Kresse, *Phys. Rev. B: Condens. Matter Mater. Phys.*, 1999, **59**, 1758.

- 24 J. P. Perdew, K. Burke and M. Ernzerhof, *Phys. Rev. Lett.*, 1996, **77**, 3865.
- 25 J. P. Perdew, K. Burke and M. Ernzerhof, *Phys. Rev. Lett.*, 1997, **78**, 1396.
- 26 Y. Wang, J. Lv, L. Zhu and Y. Ma, *Phys. Rev. B: Condens. Matter Mater. Phys.*, 2010, **82**, 094116.
- 27 J. Heyd, G. E. Scuseria and M. Ernzerhof, *J. Chem. Phys.*, 2003, **118**, 8207.
- 28 A. Togo, F. Oba and I. Tanaka, *Phys. Rev. B: Condens. Matter Mater. Phys.*, 2008, **78**, 134106.
- 29 J. VandeVondele, M. Krack, F. Mohamed, M. Parrinello, T. Chassaing and J. Hutter, *Comput. Phys. Commun.*, 2005, **167**, 103.
- 30 A. S. Sharipov, B. I. Loukhovitski and A. M. Starik, *Eur. Phys. J. D*, 2015, **69**, 211.
- 31 C. Foroutan-Nejad, G. H. Shafiee, A. Sadjadi and S. Shahbazian, *Can. J. Chem.*, 2006, **84**, 771.
- 32 Z. Zhang, X. Liu, B. I. Yakobson and W. Guo, *J. Am. Chem. Soc.*, 2012, **134**, 19326.
- 33 C.-S. Liu, H.-H. Zhu, X.-J. Ye and X.-H. Yan, *Nanoscale*, 2017, **9**, 5854.
- 34 M. Wu, Y. Pei and X. C. Zeng, *J. Am. Chem. Soc.*, 2010, **132**, 5554.
- 35 L.-M. Yang, E. Ganz, Z. Chen, Z. X. Wang and P. Schleyer, *Angew. Chem., Int. Ed.*, 2015, **54**, 9468.
- 36 J. Li, Y. P. Wei, X. Y. Fan, H. B. Wang, Y. Song, G. Chen, Y. Y. Liang, V. Wang and Y. Kawazoe, *J. Mater. Chem. C*, 2016, **4**, 9613–9621.
- 37 L.-M. Yang, V. Bacic, I. A. Popov, A. I. Boldyrev, T. Heine, T. Frauenheim and E. Ganz, *J. Am. Chem. Soc.*, 2015, **137**, 2757.
- 38 L.-M. Yang, I. A. Popov, A. I. Boldyrev, T. Heine, T. Frauenheim and E. Ganz, *Phys. Chem. Chem. Phys.*, 2015, **17**, 17545.
- 39 L.-M. Yang, I. A. Popov, T. Frauenheim, A. I. Boldyrev, T. Heine, V. Bacic and E. Ganz, *Phys. Chem. Chem. Phys.*, 2015, **17**, 26043.
- 40 L.-M. Yang and E. Ganz, *Phys. Chem. Chem. Phys.*, 2016, **18**, 17586.
- 41 B. Song, Y. Zhou, H. M. Yang, J. H. Liao, L.-M. Yang, X. B. Yang and E. Ganz, *J. Am. Chem. Soc.*, 2019, **141**, 3630.
- 42 A. Janotti, S.-H. Wei and D. J. Singh, *Phys. Rev. B: Condens. Matter Mater. Phys.*, 2001, **64**, 174107.
- 43 Y. Miyamoto, M. L. Cohen and S. G. Louie, *Phys. Rev. B: Condens. Matter Mater. Phys.*, 1995, **52**, 14971.
- 44 I. A. Popov and A. I. Boldyrev, *J. Phys. Chem. C*, 2012, **116**, 3147.
- 45 H. Sirringhaus, *Adv. Mater.*, 2005, **17**, 2411.
- 46 L. Li, G. J. Ye, V. Tran, R. Fei, G. Chen, H. Wang, J. Wang, K. Watanabe, T. Taniguchi, L. Yang, X. H. Chen and Y. Zhang, *Nat. Nanotechnol.*, 2015, **10**, 608.
- 47 X. Xuan, Z. Zhang and W. Guo, *Nanoscale*, 2018, **10**, 7898.
- 48 D. Y. Zubarev and A. I. Boldyrev, *Phys. Chem. Chem. Phys.*, 2008, **10**, 5207.
- 49 I. A. Popov, K. V. Bozhenko and A. I. Boldyrev, *Nano Res.*, 2012, **5**, 117.
- 50 T. R. Galeev, Q. Chen, J. C. Guo, H. Bai, C. Q. Miao, H. G. Lu, A. P. Sergeeva, S. D. Li and A. I. Boldyrev, *Phys. Chem. Chem. Phys.*, 2011, **13**, 11575.
- 51 X. Ling, Sh. Huang, E. H. Hasdeo, L. Liang, W. M. Parkin, Y. Tatsumi, A. R. T. Nugraha, A. A. Puzos, P. M. Das, B. G. Sumpter, D. B. Geohegan, J. Kong, R. Saito, M. Drndic, V. Meunier and M. S. Dresselhaus, *Nano Lett.*, 2016, **16**, 2260.
- 52 X. Li, Z. Li and J. Yang, *Phys. Rev. Lett.*, 2014, **112**, 018301.
- 53 M. Ashton, S. B. Sinnott and R. G. Hennig, *Appl. Phys. Lett.*, 2016, **109**, 192103.
- 54 X. Luo, G. Wang, Y. Huang, B. Wang, H. Yuan and H. Chen, *Phys. Chem. Chem. Phys.*, 2017, **19**, 28216.
- 55 Y. Zhao, Y. Lin, G. Wang, Z. Jiang, R. Zhang and C. Zhu, *Appl. Surf. Sci.*, 2019, **463**, 809.
- 56 X. Tan, Y. Ji, H. Dong, M. Liu, T. Hou and Y. Li, *RSC Adv.*, 2017, **7**, 50239.
- 57 J. J. Liu, *J. Phys. Chem. C*, 2015, **119**, 28417.
- 58 J. Kang, S. Tongay, J. Zhou, J. Li and J. Wu, *Appl. Phys. Lett.*, 2013, **102**, 012111.
- 59 R. Marschall, *Adv. Funct. Mater.*, 2014, **24**, 2421.
- 60 X. Yang, Y. Ding and J. Ni, *Phys. Rev. B: Condens. Matter Mater. Phys.*, 2008, **77**, 041402(R).